Dominant Factors Controlling the Initiation of Hydrogen Embrittlement in Al-Zn-Mg Alloy

Toda, Hiroyuki
Department of Mechanical Engineering, Kyushu University

Hirayama, Kyosuke
Department of Materials Science and Engineering, Kyoto University

Yamaguchi, Shogo
Department of Mechanical Engineering, Kyushu University

Fujihara, Hiro
Department of Mechanical Engineering, Kyushu University

他

出版情報：Materials transactions. 64 (12), pp.2729-2738, 2023-12-01. The Japan Institute of Light Metals
バージョン：

Materials Transactions, Vol. 64, No. 12 (2023) pp. 2729 to 2738

Dominant Factors Controlling the Initiation of Hydrogen Embrittlement in Al–Zn–Mg Alloy

Hiroyuki Toda[1,*], Kyosuke Hirayama[2], Shogo Yamaguchi[1], Hiro Fujihara[1], Ryota Higa[1], Kazuyuki Shimizu[3], Akihisa Takeuchi[4] and Masayuki Uesugi[4]

[1]*Department of Mechanical Engineering, Kyushu University, Fukuoka 819-0395, Japan*
[2]*Department of Materials Science and Engineering, Kyoto University, Kyoto 606-8501, Japan*
[3]*Department of Physical Science and Materials Engineering, Iwate University, Morioka 020-8551, Japan*
[4]*Japan Synchrotron Radiation Research Institute, Sayo-gun, Hyogo 679-5198, Japan*

Surrogate-based microstructural optimization was applied to model the relationship between local crystallographic microstructure and intergranular hydrogen embrittlement in an Al–Zn–Mg alloy, and a support vector machine with an infill sampling criterion was used to realise high-accuracy optimisation with a limited data set. This methodology integrates thoroughgoing microstructural quantification, two coarsening processes, and surrogate modelling. An objective function was defined together with 66 design parameters that quantitatively express size, shape, orientation and damage during specimen machining for surface grain boundaries and grains. The number of design parameters was then reduced from 66 to 3 during the two-step coarsening process. It has been clarified that intergranular crack initiation can be described using the simple size of grains and grain boundaries together with grain boundary orientation with respect to the loading direction. It can be inferred that these design parameters are of crucial importance in crack initiation through elevation in stress normal to grain boundaries. Correlation between the selected design parameters and crack initiation was somewhat weak compared to past applications of a similar technique to particle damage. The reason for this is discussed. The present approach offers a cost-efficient solution for the prevention of hydrogen embrittlement through 3D design of crystallographic microstructure that cannot be obtained using conventional strategies for developing materials.
[doi:10.2320/matertrans.MT-M2023116]

(Received July 26, 2023; Accepted September 19, 2023; Published October 6, 2023)

Keywords: *Al–Zn–Mg alloy, hydrogen embrittlement, X-ray tomography, diffraction contrast tomography, intergranular fracture, statistical analysis, surrogate model, support vector machine, data coarsening*

1. Introduction

It is usually observed when hydrogen embrittlement occurs that three fracture modes exist: intergranular fracture, accelerated transgranular fracture with the hydrogen-enhanced localized plasticity (HELP) mechanism, and transgranular quasi-cleavage fracture.[1)] It is also known that hydrogen is precipitated as high density micropores that accelerate transgranular ductile fracture.[2–4)] The three fracture modes, which are intergranular fracture, transgranular quasi-cleavage fracture and the growth and coalescence of pre-existing micropores, commonly occur at the same time and interact both in time and space.

Tsuru *et al.*, performed a first-principles simulation in which multiple hydrogen atoms were located at the coherent interface between η precipitates and the aluminium matrix in an Al–Zn–Mg alloy. It was demonstrated that interfacial cohesive energy gradually decreases with increased hydrogen concentration, and finally reduced to zero.[5)] It is interesting to note that a precipitate/matrix interface is gradually opened with an increase in interfacial hydrogen concentration.[5)] The present authors refer to this as semi-spontaneous interfacial debonding. It has been explained in physical terms that the interfacial binding energy between precipitates and the matrix is lower in aluminium than in other metals such as steels, and any high surface trapping energy due to the dissociative adsorption of hydrogen is compensated for the energy of fracture surface formation. This process reveals the nanoscopic mechanism and quantitative initiation conditions, which have not hitherto been elucidated, for transgranular quasi-cleavage fracture. The present authors performed 3D image-based simulations to investigate the growth of hydrogen embrittlement cracks by utilising the critical hydrogen concentration for semi-spontaneous interfacial debonding to occur.[6)] Mutual interaction effects among crystallographic grains are superimposed on a crack-tip hydrostatic stress field to generate high hydrostatic tension.[6)] Hydrogen can segregate here relatively short time and reaches the critical interfacial hydrogen concentration needed for semi-spontaneous interfacial debonding to occur. We have previously concluded that the growth of quasi-cleavage cracks is effectively explained by the occurrence of semi-spontaneous interfacial debonding.[6)]

A similar approach has been applied to crack initiation caused by hydrogen embrittlement.[7)] It has been concluded that the crystallographic microstructure alone causes a limited increase in hydrostatic stress, but this approach does not predict the hydrogen concentration needed for crack initiation.[7)] It has been reported in connection with intergranular hydrogen embrittlement that numerous intergranular cracks may sometimes be formed simultaneously in materials that are highly susceptible to hydrogen embrittlement in high hydrogen atmospheres,[8)] while only a few cracks may sometimes be observed.[9,10)] It has been directly observed, using 3D atom probe tomography technique that hydrogen concentrates along grain boundaries.[11,12)] It has been reported that hydrogen segregation occurs at triple junction points.[12)] It has also been thought that intergranular fractures occur due to weakened atomic bonding caused by hydrogen segregation.[13)] Particularly in the case of aluminium, it has been predicted by Yamaguchi *et al.*, using a first-principles simulation, that similar to the precipitate/matrix

*Corresponding author, E-mail: fujihara@mech.kyushu-u.ac.jp

interface, intergranular cohesive energy vanishes due only to hydrogen segregation, which thereby causes semi-spontaneous intergranular debonding.[14] Needless to say, grain boundaries never exhibit complete spontaneous debonding, so it is reasonable to conclude that semi-spontaneous intergranular debonding occurs in a form in which brittle intergranular fractures, which are usually assumed to act as stress control, are accelerated by the effects of hydrogen.[15] As a result, the effects of material strength are clearly evident.[15] Embrittling elements at grain boundaries promote intergranular fracture, as with the cases of Mn and Si in steels.[15] Conversely, elements exist that suppress intergranular fractures caused by the presence of hydrogen, as in the case of carbon along prior austenite grain boundaries in steels.[16] It is also known that hydrogen segregation is dependent on grain boundary character, which strongly affects resistance to hydrogen embrittlement.[13] It appears that low energy grain boundaries with high coherency and small free volume are immune to hydrogen embrittlement.[13,17,18] The grain size dependency of hydrogen embrittlement susceptibility also appears to be well known.[19,20] While various results have been reported from experiments that focus on highly efficient microstructural control, it is of crucial importance to comprehensively evaluate and elucidate which microstructural factors control intergranular fractures and to what extent.

The present authors have proposed a method that we term 'Reverse 4D materials engineering', by which statistical correlations between microstructures and macroscopic properties are comprehensively evaluated and analysed.[21,22] Using this method, a correlation between design parameters that describe microstructural morphology, and objective functions that describe macroscopic material behaviour is obtained by percomprising numerical simulations using 3D image-based models that reproduce captured 3D information on a material's microstructure with high fidelity. We intentionally adopt redundant quantification by describing microstructural morphology using dozens of design parameters in response to the complexity of the microstructures of real materials and limited imaging properties. In a subsequent coarsening process, a restricted number of design parameters that are highly correlated with objective functions are identified, and a metamodel is constructed to express this correlation. Since the series of analyses is based on high fidelity 3D images, normally sophisticated microstructural control is realised with regard to fine surface morphology and particle clustering. This was utilised to evaluate the effects of dispersed particles and microscopic defects on damage and fracture behaviour in high-strength aluminium alloy: we successfully identified several dominant factors that create damage to visualise the dependency of damage behaviour on microstructures, and at the same time identified the optimum/weakest microstructures.[21,22]

In this study, a multi-modal technique was established by combining diffraction contrast tomography[23,24] for 3D observation of polycrystalline microstructure with high resolution 4D observation of intergranular cracks to record hydrogen embrittlement crack initiation behaviour from hundreds of surface grains. By applying 4D reverse materials engineering to this data, the dominant microstructural factors controlling intergranular fracture were identified from various features of fractured grain boundaries. We aimed to visualise the dependency of intergranular fractures on polycrystalline microstructure together with the identification of the weakest and strongest microstructures to hydrogen embrittlement.

2. Experimental and Analytical Methods

2.1 4D observation of hydrogen embrittlement behaviour

2.1.1 Materials used

An Al–10Zn–1.06Mg (mass%) pure ternary alloy was prepared in the laboratory. The concentrations of impurity elements (Si, Cu, Mn, Cr and Ti) were 0.005, 0.016, 0.001, 0.001, 0.018 mass%, respectively. After casting, the material was homogenized at 773 K for 2 h, hot-rolled at 723 K, solution-treated at 773 K for 2 h, followed by quenching in ice water, and finally artificially two-step aged at 393 K for 40 h and 453 K for 7 h. After that, micro specimens were sampled by electric discharge machining in water, which also serves as hydrogen charging. The specimen geometry is the same as in the literature.[25] It has been reported that electrical discharge machining performed in water increases the hydrogen content of similar aluminium alloys by a factor of 50.[26] To allow the charged hydrogen to sufficiently diffuse into the samples, the samples were held at room temperature for 96 hours after electrical discharge machining and before tensile testing. The hydrogen concentration of the tested material was measured by employing thermal desorption analysis. A high hydrogen concentration of 6.85 mass ppm was obtained at 1.5°C/min up to 580°C.

2.1.2 *In-situ* observation of tensile tests under synchrotron X-ray

In-situ observation of the tensile tests was performed at BL20XU at SPring-8, a highly brilliant synchrotron radiation facility, using projection-type X-ray CT. The obtained 3D image had isotropic voxels of 0.50 μm edge and a substantial spatial resolution of 1.0 μm. The X-ray energy was 20 keV, and sample-to-detector distance was 20 mm. Tensile displacement was applied to specimens in an argon flow environment. Displacement was held for 15 minutes before X-ray CT imaging for every 0.01 mm increment in displacement. To obtain statistically significant data, the tensile test was repeated under the same conditions with seven specimens and the data was pooled. Convolutional backprojection was used for reconstruction, and the grayscale range of the 8-bit images was set to between 0 and 40 cm^{-1} as the linear absorption coefficient.

Before tensile loading, polycrystalline grain images and crystal orientation distributions in the gauge sections of the specimens were obtained by diffraction contrast tomography (DCT). Diffraction spots from the (111), (200), and (220) planes of aluminium were acquired at an X-ray energy of 30 keV using a CMOS detector that was placed 6 mm behind the sample. The samples were rotated 360° to utilise Friedle pairs for reconstruction to eliminate the effects of double diffraction. Note that the DCT measurement was performed only before loading, because reconstruction is greatly degraded due to diffraction spot blurring when a load is applied.

2.2 Image analysis

2.2.1 Registration between crack and grain images

In the material tested, cracks were initiated after a certain degree of plastic deformation. It is therefore not possible to accurately register a polycrystalline grain image captured using DCT in the initial unloaded state with a crack image captured after the plastic deformation of the specimen, by which crack initiation sites (are they intergranular or transgranular? On which grain boundary, grain boundary triple line or grain boundary quadruple point are located?) are not precisely identified. We estimated crack position and shape for the initial unloaded state by applying the fracture path prediction technology developed in previous studies[2,3] to register it with a polycrystalline grain image obtained before loading.

2.2.2 Metamodeling for crack initiation

In this study, we employed the surrogate-based optimization method proposed in our previous study.[21,22] To quantitatively express the morphologies of a polycrystalline microstructure, three categories were established: the surface grain boundary, the pair of grains that form a surface grain boundary, and the three surface grains that form a triple junction point. Design parameters for grains and grain boundaries that represent the size, shape, orientation, and crystallographic orientation (i.e., Schmid factor and local Taylor factor) were prepared. Only those design parameters that had a small interdependence between the design parameters and a high correlation with an objective function (i.e., resistance to intergranular crack initiation) were then extracted. A meta-model was constructed using the extracted design parameters, and the relationships between the properties of the polycrystalline microstructure and resistance to intergranular fracture were visualised. Principal component analysis was employed to eliminate design parameters that showed interdependence, followed by global sensitivity analysis to assess the correlation. In this study, several tens of intergranular cracks originating from hundreds of grain boundaries were analysed. Since the number of data points was too small to permit statistical analysis, a support vector machine with infill sampling criteria was used to construct the metamodel that enables a highly accurate analysis to be performed based on a limited data set. The details of the method are available elsewhere.[21,22] Here, the details of the design parameters and an objective function, which differ from those reported previously, are described below.

(1) Details of design parameters

The categories of the design parameters that represent grain boundary properties are surface grain boundary (hereinafter SG), two surface grains that form a surface grain boundary (hereinafter GP), and three surface grains that form a grain boundary triple junction (hereinafter TJ). A brainstormed list of possible design parameters was prepared for each category. Table S1 shows a list of all the design parameters used.

For category SG, five design parameters were prepared: grain boundary area, orientation angle defined by the angle between the loading direction and a grain boundary normal, aspect ratio, average curvature, and pore density in the vicinity of a grain boundary. Here, micropores formed by the clustering of hydrogen atoms tend to form on or in the vicinity of grain boundaries, and are therefore added to the design parameters because they may affect hydrogen embrittlement behaviour.

Strain localization in the vicinity of grain boundaries is attributable to deformation mismatch between grains sandwiching grain boundaries. We therefore presume that the properties of the crystallographic grains comprising the grain boundaries have a significant influence. In category GP, the ratios of two grains in volume, average curvature, number of adjacent grains, spherical deviation, cubic deviation, local Taylor factor, Schmid factor and relative misorientation between grains were prepared. The definitions of spherical and cubic deviations are given in previous reports.[21,22] Calculation of the local Taylor factor requires the 3D strain distribution inside a material. In the gauge sections of the specimens, there are 15,738 to 20,289 micropores that exhibit physical displacements under external loading. Therefore, by measuring the physical displacements of all the micropores, local strain distribution due to external loading can be measured. Details of the method are available elsewhere.[24,27] In addition to these design parameters, the cutoff rate was defined. The crystallographic grains that are located on the specimens' surfaces are somewhat smaller than their original size due to cutting and/or polishing during the specimen preparation process. The definition of cutoff rate is the volume ratio of the portion remaining and the crystallographic grain volume before cutting. In this case, it is impossible to predict the shape of the surface crystal grains before specimen preparation. We randomly selected 12 perfect grains that were completely embedded inside the specimens. The change in cross-sectional area was measured by utilising the 3D images obtained when the grains were gradually worn away from the perfect grains during cutting, as shown in Fig. 1, and utilised as a calibration curve. The cutoff rate of each surface crystallographic grain was calculated from the reduction rate in its cross-sectional area that was obtained by dividing the cross-sectional area of the grain on the surface by that of the cross section 3 μm below

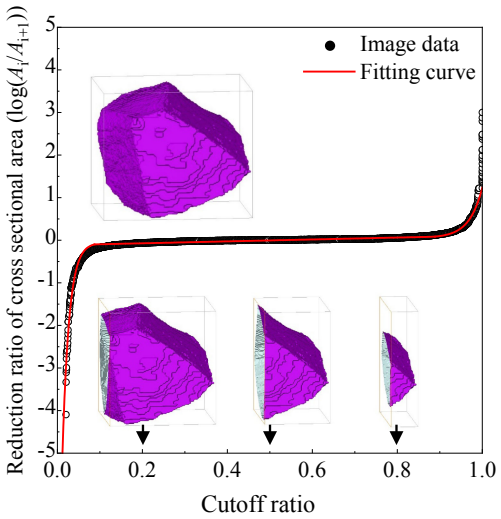

Fig. 1 Relationships between grain cutoff ratio and the reduction rate of grain cross-sectional area. The black dots are data acquired from grains located inside of the specimen. The red line is a fitting curve for the black dots.

the surface. Since crystallographic grains positioned at the corners of the specimens were cut-off from two directions, the corner cutoff rate, S_{corner}, was defined as follows.

$$S_{corner} = 1 - \{(1 - S_1)(1 - S_2)\} \quad (1)$$

where the cutoff rates in the two directions are S_1 and S_2, respectively.

Figure S1 shows the results of the cutoff rate calculations for all the 214 surface grains observed in the gauge sections of the seven specimens.

There are two grain boundary triple junction lines that reach the surface for one surface grain boundary. Therefore, for each design parameter in category TJ, one of the two grain boundary triple junction lines that had a larger value in a design parameter of interest was adopted as the value of the grain boundary. The maximum, mean, and ratio of the maximum and mean of three grains were measured in Category TJ for volume, aspect ratio, mean curvature, spherical deviation, cubic deviation, local Taylor factor, Schmidt factor, relative misorientation, and cutoff rate.

A total of 66 design parameters (5 for SG, 16 for GP, and 45 for TJ) were used to comprehensively express the properties of surface grain boundaries.

(2) Details of objective function

For all the surface grain boundaries, the applied strain at which crack initiation was observed during the *in-situ* observation of tensile tests was used as an index of the susceptibility to hydrogen embrittlement at each surface grain boundary. The presence or absence of an initiated intergranular crack was defined such that the objective function was set at unity if a grain boundary was not fractured up to the maximum load placed on of each sample, and 0 if a crack was observed. For the grain boundaries where a crack was initiated, a value between 0 and 1 was assigned as the value of the objective function using the nominal strain of the loading step at which crack initiation was observed for the first time, with 20% applied strain being 1 and 0% being 0. Note that the maximum applied strain at which crack initiation was actually observed was 8.6%.

3. Results of 4D Observation of Hydrogen Embrittlement Behaviour

Figure 2(a) shows the 3D polycrystalline grains image of specimen No. 1 of the seven specimens tested before loading. A total of 34 grains were observed between the specimen gauge section, and 234 grains were observed in the gauge section of the seven specimens. Of these, 208 grains appeared on the surface. The 535 grain boundary planes were located on the surface together with 324 grain boundary triple junction lines. The polycrystalline structure is judged to be precisely visualised, as there are no gaps or overlaps between the grains due to measurement errors, and the grain boundaries and the cracks measured by X-ray CT coincide without deviation.

The load-displacement curve obtained during the tensile testing of specimen No. 1 is shown in Fig. 3; the six stress drops observed in Fig. 3, each about 10 N, are due to stress relaxation caused by holding displacement during the X-ray

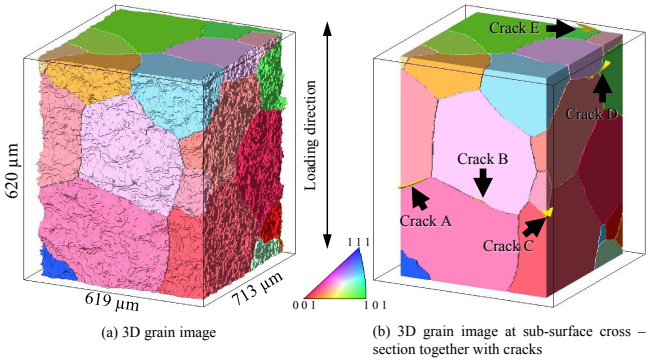

Fig. 2 (a) 3D grain and orientation images for specimen No. 1 that were obtained using DCT. (b) Superimposition of the 3D grain image and a 3D crack image. Cracks are highlighted in yellow.

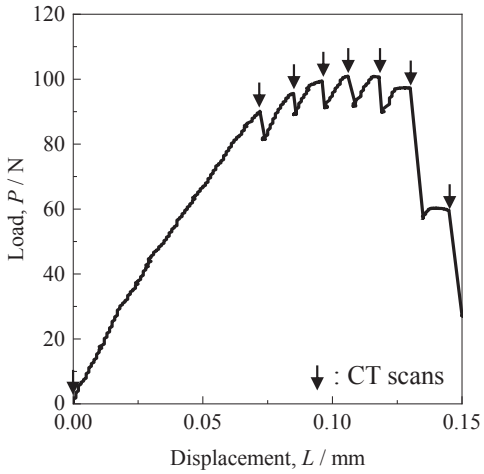

Fig. 3 Load-displacement curve recorded during the *in situ* tensile testing of specimen No. 1.

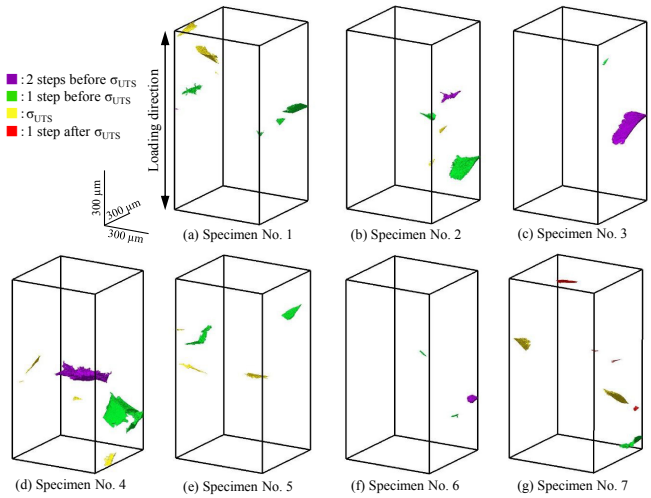

Fig. 4 Intergranular cracks that were observed in the vicinity of the maximum tensile strength in the seven specimens. Cracks were color-coded according to the loading stages at which crack initiation is observed.

CT observations. In Fig. 4, the 41 cracks that were observed in the vicinity of the maximum tensile strength in the seven specimens are colour-coded according to the loading stage of

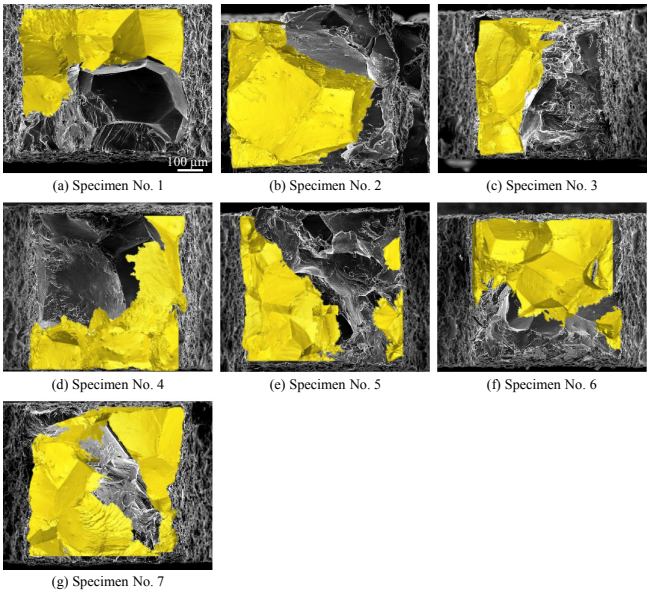

Fig. 5 Superposition of the SEM fractographs (black and white) and the 3D crack images, highlighted in yellow, that are obtained near maximum loads.

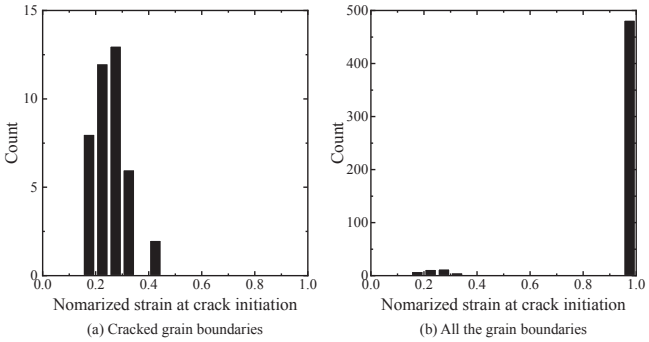

Fig. 6 Normalized crack initiation strain for (a) grain boundaries that exhibited intergranular fracture and (b) all the grain boundaries.

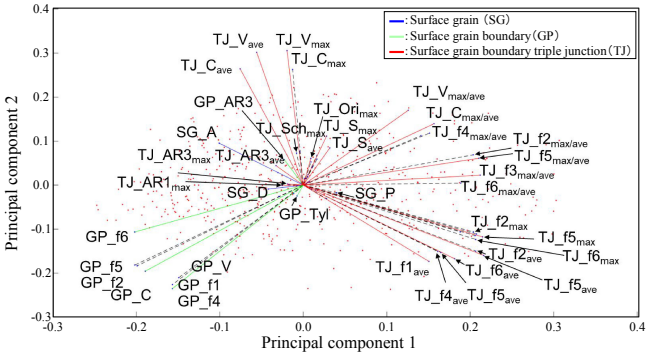

Fig. 7 Principal component score distribution for all the design parameters.

crack initiation. Cracks that were initiated at the maximum load and one loading step before the maximum load were both present in about 40% of the cases, while those that occurred after one step of the maximum load and before two steps of the maximum load were both present in about 10% of the cases.

Crack images in the initial unloaded state were estimated using the method described in section 2.2.1 and superimposed on the polycrystalline grains image also captured in the initial unloaded state as shown in Fig. 2(b). Figure 5 is a superimposition of the SEM images (black and white) of the fracture surface of seven specimens and the 3D cracks image (yellow) observed up to around the maximum loads by employing the X-ray CT technique. By the maximum load point, between 40% and 70% of the fracture surface has already been formed. This means that the material tests in this study are not general tensile tests where damage occurs around the maximum load, but rather an assessment of crack initiation and crack propagation resistance with R-curve behaviour. Note that near the maximum loads, most of the 41 cracks have grown sufficiently and coalesced with neighbouring cracks. Although there were features of ductile fracture and intragranular quasi-cleavage fracture on the fracture surfaces, all the 41 cracks originated from the surface grain boundaries as intergranular cracks. The dimensionless crack initiation strain defined as the objective function in Section 2.2.2(2) is shown only for the grain boundaries that exhibited intergranular fracture in Fig. 6(a). Figure 6(b) includes the data for the grain boundaries that did not fracture.

4. Results of Metamodel Analysis of Crack Initiation

Figure 7 is a biplot that illustrates the principal component vectors and scatter plots in the principal component analysis. The blue, green and red lines respectively represent the design parameters SG, GP and TJ. In this study, the design parameter with the smaller contribution was eliminated when the angle between the principal component vectors of each design parameter pair was less than 5°. The black dashed lines in the figure indicate the design parameters eliminated in this way. The initial number of design parameters was 66, and after application of the principal component analysis, the number was reduced to 25. The number of remaining design parameters was 3, 5 and 17 for categories SG, GP and TJ respectively, with SG remaining in the highest proportion (60%), while GP remained to an intermediate degree.

A global sensitivity analysis was applied to the 25 design parameters that passed the first stage of the coarsening process. They are listed in order of Pearson correlation coefficient in Fig. 8, colour-coded according to the categories of design parameters SG, GP and TJ in Fig. 8(a) and according to grain boundary properties such as crystallographic orientation, size, shape and cutoff rate in Fig. 8(b). In a previously published study[21] that used a similar method to examine the correlation between the properties of individual dispersed particles in aluminium and their damage, the average of the top three Pearson correlation coefficients ranged from 0.27 to 0.56, while in the study that also analysed the properties and arrangement of dispersed particles in a 40 μm cubic region in aluminium,[22] the top three averages ranged from 0.62 to 0.72. In Fig. 8, the average of the top three Pearson correlation coefficients was 0.15, which is assumed to be relatively low compared to the previous reports. This is discussed later in the paper.

In Fig. 8(a), the Pearson correlation coefficient values are higher for category SG, followed by TJ. The top three design

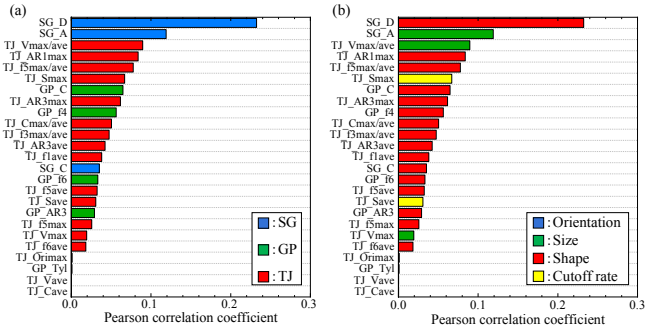

Fig. 8 The results of the global sensitivity analysis for the selected 25 design parameters. The bars are color-coded according to (a) the categories of design parameters SG, GP and TJ, and (b) classification such as crystallographic orientation, size, shape and cutoff rate.

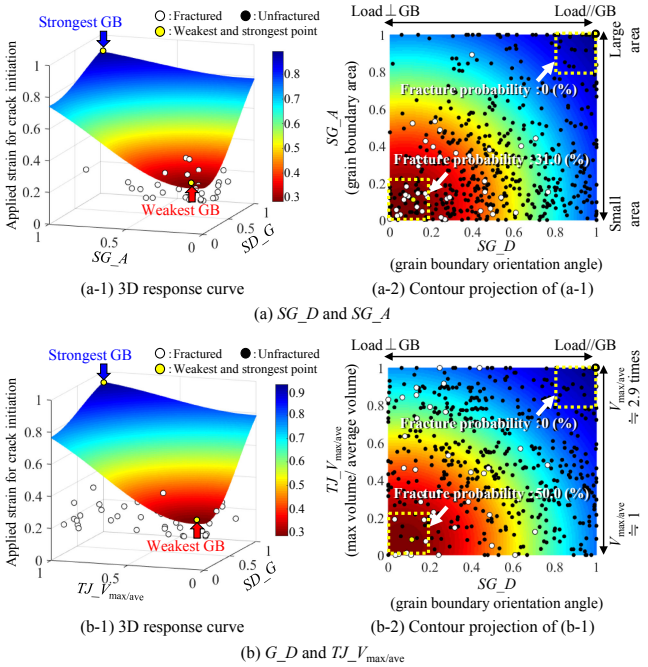

Fig. 9 3D response surfaces among the two design parameters ((a) *SG_D* and *SG_A* and (b) *G_D* and *TJ_V*$_{max/ave}$) and the objective function together with projected 2D contour representation of the objective function.

parameters are the grain boundary orientation angle of a single grain boundary (*SG_D*), grain boundary area (*SG_A*), and the maximum value of the volume of the three grains comprising a surface grain boundary triple junction line divided by their average (*TJ_V*$_{max/ave}$). It is characteristic that Fig. 8(b) shows very small values for the design parameters related to crystallographic orientation. The importance of the cutoff rate ratio was also low. Those related to the size and shape of grain boundaries and grain survived. In other words, what controls intergranular fracture is not a crystallographic mismatch of the polycrystalline microstructure or the partial loss of surface grains at the sample preparation stage, but simply the geometrical factors of the grains and grain boundaries.

A metamodel was created using *SG_D*, *SG_A* and *TJ_V*$_{max/ave}$. To evaluate the correlation in a visually intuitive manner, response surfaces for the objective function were drawn using only *SG_D* and *SG_A* in Fig. 9(a) and only *SG_D* and *TJ_V*$_{max/ave}$ in Fig. 9(b). In the former and latter, the response surfaces were drawn with constant average values of *SG_A* and *TJ_V*$_{max/ave}$, respectively. Figure 9 shows a 3D response surface among the two design parameters and the objective function together with a 2D contour representation of the objective function. The weakest grain boundary with regard to hydrogen embrittlement is that with a small grain boundary area (5.6×10^3 μm^2: 1.8×10^4 μm^2 on average for all the grains), grain boundaries orientated perpendicular to the loading axis (88.4°: 48.0° on average for all the grains) and a grain boundary triple junction line where the volume of the three grains surrounding it was relatively close (1.41 for *TJ_V*$_{max/ave}$ before normalization: 2.09 on average for all grains). Conversely, the strongest grain boundary against hydrogen embrittlement was found to have a large grain boundary area (5.1×10^4 μm^2). The grain boundary was close to parallel to the loading axis (16.2°) and there was a significant volume difference among the three grains surrounding the grain boundary triple junction line (2.86 before normalisation of *TJ_V*$_{max/ave}$).

In the 2D contour plots in Fig. 9(a) and (b), the black dots indicate the grain boundaries that did not fracture, the white dots indicate the fractured grain boundaries, and the two yellow dots indicate the predicted positions of the weakest and strongest grain boundaries. There are a number of grain boundaries near the weakest grain boundary that did not fracture, and conversely, there are fractured grain boundaries near the centre of the figure that are relatively close to the strongest grain boundary. Here, the weakest grain boundary is defined as the grain boundary with the highest predicted probability of fracture, while the strongest grain boundary behaves in the opposite way. Regions surrounding the weakest and optimum points were set as shown by the yellow dotted lines in the 2D contour diagrams in Fig. 9(a) and (b), and the fracture probability of grain boundaries inside the regions was calculated. The results showed the fracture probability near the weakest point to be as high, at 31.0% and 50.0% in Fig. 9(a) and (b), respectively, whereas it was 0% near the optimum point.

For reference, the grain boundaries with *SG_D* and *SG_A* values closest to the weakest and strongest grain boundaries in Fig. 9(a) are extracted in Fig. 10(a) from the 234 grains actually observed in the seven specimens. Figure 10(b) also shows the extracted grain boundaries with *SG_D* and *TJ_V*$_{max/ave}$ values closest to the weakest and strongest grain boundaries in Fig. 9(b). Referring to the results of Higa *et al.*,[7] who performed a 3D image-based crystal plasticity finite element analysis on similar materials, the stress normal to a grain boundary varies greatly according to the grain boundary orientation angle and grain boundary area, and the strongest grain boundary possesses small values in these design parameters. If there is a coarse grain in three grains surrounding a grain boundary triple junction line, smaller grains deform following the coarse grain, thereby limiting the mismatch among them. Conversely, if three grains surrounding a grain boundary triple junction line are of similar size, it is assumed that the mismatch in deformation among the grains increases due to mutual deformation constraint effects, resulting in a higher grain boundary stress.

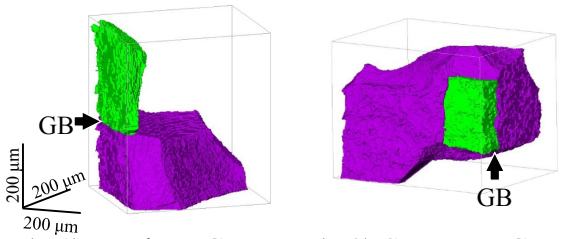

(a-1) Weakest GB (a-2) Strongest GB

(a) *SG_D* and *SG_A* values closest to the weakest and strongest grain boundaries

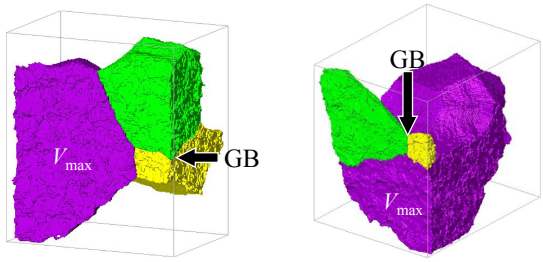

(b-1) Weakest GB (b-2) Strongest GB

(b) *G_D* and *TJ_*$V_{max/ave}$ values closest to the weakest and strongest grain boundaries

Fig. 10 3D images of grains constituting grain boundaries that are close to the weakest and strongest grain boundaries in Fig. 9.

5. Discussion

5.1 Microstructure-fracture behaviour correlation

Yamaguchi *et al.* performed first-principles calculations while increasing hydrogen concentration at the interface between Σ5(012), Σ9(221) and Σ3(112) grain boundaries. A peculiar behaviour is seen, in which the grain boundary expands due to the presence of multiple hydrogen atoms, causing stabilization by trapping more hydrogen atoms at the grain boundary.[14] As mentioned above, an increase in the hydrogen concentration at a grain boundary leads to semi-spontaneous interfacial debonding, where grain boundary cohesive energy decreases to nearly zero.[14] On the other hand, the results of an image-based analysis performed by Su *et al.* show that in Al–Zn–Mg alloys, hydrogen is overwhelmingly partitioned to precipitates and micropores, with the proportion of hydrogen trapped by grain boundaries being only 10^{-4} to 10^{-5} of that trapped in precipitates and micropores.[28] This is true for both the initial unloaded state and regions are loaded heavily ahead of a crack. Therefore, if intergranular fracture occurs according to the semi-spontaneous interfacial debonding mechanism, the effects of hydrogen appear to be only supplementary, and an increase in the stress on a grain boundary is essential for hydrogen embrittlement to occur.

Higa *et al.* performed 3D image-based multimodal simulations, coupling the crystal plasticity finite element method and hydrogen diffusion analysis for an Al–Zn–Mg alloy with a composition similar to that of the present material (the average grain size is slightly smaller, at 160 μm) to examine the relationship between intergranular crack initiation due to hydrogen embrittlement and stress/strain localisation and hydrogen concentration.[7] An increase of 8.3 times the average in equivalent plastic strain, 3.7 times in hydrostatic stress and 2.3 times in stress normal to a grain boundary was observed at certain grain boundaries. This trend was particularly pronounced at certain grain boundaries that exhibited crack initiation. Hydrogen accumulation is predicted in the vicinity of the surface of certain grain boundaries in response to elevated tensile hydrostatic stress. They concluded that the higher the stress normal to a grain boundary, the more likely intergranular cracking is to occur, and that the stress normal to a grain boundary outweighs the effects of hydrogen accumulation due to elevated hydrostatic stress.[7] This is consistent with the results of the present study, in which *SG_D*, *SG_A* and *TJ_*$V_{max/ave}$ as dominant design parameters were highly correlated with intergranular fracture, predicting the strongest and weakest microstructures shown in Figs. 9 and 10.

The values of the Pearson correlation coefficients for the three selected design parameters *SG_D*, *SG_A* and *TJ_*$V_{max/ave}$ were 0.23, 0.12 and 0.09 respectively. According to Evans, the Pearson correlation coefficient values of 0.8–1.0, 0.60–0.79, 0.40–0.59, 0.20–0.39, and 0–0.19 respectively correspond to very strong, strong, moderate, weak and very weak correlations.[29] *SG_D* is therefore judged to be weakly correlated with intergranular fracture, and *SG_A* and *TJ_*$V_{max/ave}$ to be very weakly correlated. On the other hand, previously reported Pearson correlation coefficient values obtained using a similar method for the relationship between the damage susceptibility of individually dispersed particles in aluminium and the properties of the dispersed particles ranged from 0.27 to 0.56,[21] indicating a weak to moderate correlation. Also, in a study investigating the properties and arrangement of dispersed particles in 40 μm cubic regions,[22] the Pearson correlation coefficient was judged to be strong, ranging from 0.62 to 0.72. The reason that the correlation was weak in this study could be that the Pearson correlation coefficient for a single design parameter was low due to the macro-phenomenon being affected by a combination of more than one design parameters, or that the contribution of design parameters is little considered here.

With regard to the latter hypothesis, the image-based analysis performed by Su *et al.* concluded that the amount of hydrogen partitioned to the grain boundary itself is almost negligible, and cannot reach a critical hydrogen concentration for intergranular fracture to occur via the semi-spontaneous interfacial debonding mechanism.[28] A different intergranular fracture mechanism may therefore be dominant. Grain boundaries usually exhibit complex aspects, such as segregation of alloying elements, formation of PFZs and the presence of grain boundary precipitates, which are different from the pure grain boundaries analysed in physics-based simulations.[30] It can therefore be hypothesised that intergranular fracture is triggered by grain boundary precipitates, in the same way that transgranular quasi-cleavage fracture has been reported to be originated from the semi-spontaneous interfacial debonding of intra-grain precipitates.[5] The maximum hydrogen trap energy for grain boundaries is as low as approximately 0.25 eV,[14] whereas it is reported to be about 0.35 eV[31] and 0.55 eV[32] at coherent

and semi-coherent interfaces between η-$MgZn_2$ precipitates and the aluminium matrix, respectively. This suggests that grain boundary precipitates attract hydrogen much more strongly than does the grain boundary itself. In the case of grain boundary precipitate-dominated intergranular fractures, the size, shape, density (i.e., coverage), spatial distributions on the grain boundary and coherency of intergranular precipitates are likely to be important design parameters. Since these can be visualised in 3D by employing high-resolution-imaging X-ray CT depending on ageing state and alloy type, it can be treated in similar a way to that of the present study.

It should be noted that, in the present study, it was intended that the specimens be fully charged with hydrogen and then tested under argon flow to eliminate the influence of external hydrogen. However, since the atmosphere could not be completely replaced in advance, it is reasonable to assume that some water vapour partial pressure remains. As the specimens are deformed, the surface oxide film, which is an oxide ceramic, is destroyed and the metallic aluminium is exposed to water vapour, resulting in an oxidation reaction that produces excess hydrogen atoms. The hydrogen atoms produced are absorbed into the aluminium due to their high fugacity[33] and appear to contribute to hydrogen embrittlement. Fracture of the oxide film is thought to depend on the presence of grain boundaries and deformation mismatches between grains. It is, however, difficult to account for this behaviour based exclusively on design parameters. It is also difficult to measure the amount of hydrogen absorbed from outside. It can be inferred that if the atmosphere is completely controlled by gas replacement after evacuation, intergranular fractures will be dominated only by internal hydrogen and that the correlation with the design parameters will tend to increase.

5.2 Potential applications for grain boundary fracture control

The approach adopted in this paper explicitly characterises the weakest and strongest grain boundaries and describes the resistance to grain boundary fracture in the form of fracture probability for any grain boundaries in between. This is because the dominant microstructural factors can be extracted from a large amount of data, even if they are poorly correlated. This enables the characterization of complex phenomena and their rational interpretation. In other words, it makes it possible to shift from the traditional intuitive and subjective understanding of phenomena to a logical interpretation supported by rich data. In general, the interpretation of 3D/4D images and the use of 3D image-based numerical simulations requires specialists with a deep understanding of materials science, advanced skills and the ability to interpret information-rich data. However, if the microstructure is optimised by measuring and evaluating the dominant factors of macro phenomena using the approach taken in this research, the macro properties of materials can be efficiently improved without the need for specialists. Duplications and discrepancies can lead to erroneous conclusions. Therefore, to obtain reliable results, these problems must be corrected beforehand by data cleansing. However, the statistical methodology used in this paper can reach identical conclusions without data cleansing, no matter who runs it, as long as an appropriate objective function is set and a sufficient number of design parameters are provided. This is because the preparation of an excessive number of design parameters and the subsequent coarse-graining process inherently have a data cleansing function. The evaluation by visualisation of correlations by metamodels also allows validation of the adequacy and effectiveness of the optimisation achieved by the selected metamodel.

More specifically, based on the findings of this study, by measuring the three selected design parameters *SG_D*, *SG_A* and $TJ\_V_{max/ave}$ or equivalent design parameters with high Pearson correlation coefficients, and considering the loading direction when used as a component, susceptibility to hydrogen embrittlement due to intergranular failure can be controlled. In this case, grain boundaries close to the *SG_D*, *SG_A* and $TJ\_V_{max/ave}$ values of the weakest microstructure can be eliminated as far as possible, or grain boundaries close to the *SG_D*, *SG_A* and $TJ\_V_{max/ave}$ values of the optimum microstructure can be increased as much as possible. Considering that hydrogen embrittlement is caused by crack initiation and propagation from a limited number of grain boundaries, the former would seem to be the more effective approach. In such cases, the difference between the assumed component size and the size of grain boundary forces the use of small samples of the order of millimetres sampled from the component. Of course, the use of synchrotron radiation is often impractical for industrial materials development and evaluation. It has recently become possible for the experimental technique under synchrotron light used in this study to be performed using laboratory equipment, albeit with the disadvantages of slightly reduced accuracy and longer measurement times.[24,34] Materials with an optimum microstructure that cannot be achieved by trial and error can be created, so the application of the 3D measurement methods and the use of image-based analysis, as in the present study, would be a realistic approach.

Previous reports describe the preparation of number of simulation models by utilising, replicating or modifying specific microstructural features observed in a single specimen, and statistical analyses of the results of 3D image-based numerical simulations to statistical analysis similar to that used in the present study.[21,22] If one is sufficiently aware of the design space covered by various design parameters using realistic materials, this approach would be equivalent to battologised experimental evaluation. In such cases, if the correspondence between hydrogen concentration and crack initiation is confirmed, the predicted local hydrogen concentration, such as that obtained by Higa *et al.*'s[7] crystal plasticity finite element analysis and hydrogen diffusion analysis, can also be used as an objective function. Although 3D image-based multimodal simulations of these types are sometimes computationally expensive, they may lead to more effective polycrystalline microstructure optimisation, incorporating realistic polycrystalline microstructure changes during thermo-mechanical treatment.

6. Conclusion

A microstructural optimisation method, with metamodel-

ing as its principal component, was applied to investigate the correlation between the polycrystalline microstructure of a hydrogen embrittlement-sensitive Al–Zn–Mg alloy and crack initiation behaviour during hydrogen embrittlement. Support vector machines were combined with an infill sampling criterion to perform statistical analyses suitable for data sets with relatively small data sizes - a few hundred in terms of number of grain boundaries. Methodologically, the study integrated thorough polycrystalline microstructure quantification using a large number of design parameters, two coarse-graining processes and metamodeling. The aim of the study was to optimise the 3D polycrystalline microstructure by considering the size, shape and orientation of a surface grain boundary, a pair of surface grains comprising a surface grain boundary, and three grains comprising a surface grain boundary triple junction line. The cutoff rate of surface grains during the specimen preparation process was also considered. A total of 66 prepared design parameters were coarsened to 25 according to data independence, and finally to three according to their correlation with crack initiation during hydrogen embrittlement. Combining these three design parameters and an objective function, a four-dimensional metamodel was constructed that was visualised as a 3D or 2D response surface.

The design parameters used were those describing the size, shape and orientation of surface grain boundaries and surface grains, and the cutoff rate during the sample preparation process. Many of the design parameters describing the properties of a single grain boundary remained, while those relating to the properties of the two grains comprising the grain boundary tended to be eliminated, with the properties of the grains comprising the surface grain boundary triple junction line being in between. A similar trend was observed in the correlation analysis. The three design parameters selected were the grain boundary orientation angle of a single grain boundary (*SG_D*), the grain boundary area of a single grain boundary (*SG_A*) and the maximum volume of three grains comprising a surface grain boundary triple junction line divided by their average ($TJ\_V_{max/ave}$). The Pearson correlation coefficient values for these design parameters were significantly lower in this study than reported in previous similar studies. This suggests that the size, shape, density, spatial distribution on grain boundary and coherency of grain boundary precipitates should be taken into consideration, since grain boundary fractures appear to be triggered by grain boundary precipitates, just as transgranular quasi-cleavage fracture is caused by semi-spontaneous interfacial debonding of intra-grain precipitates. It was also inferred that the low correlation coefficient was partly due to the fact that, in this study, the influence of external hydrogen could not be completely eliminated.

As a result, the weakest grain boundaries against hydrogen embrittlement were those with a small grain boundary area, with grain boundaries orientated perpendicular to the loading axis and with three grain volumes relatively closely surrounding a grain boundary triple junction line. This is in good agreement with the results of a separate 3D image-based multimodal simulation. Using the simulation results as support, it can be understood these conditions were assumed to cause deformation constraint effects among grains, resulting in high grain boundary stress. Furthermore, the crystallographic structures that were the most resistant and the weakest crystallographic structures to hydrogen embrittlement were identified from 3D images of the actual material and used as examples. The elimination, as far as possible, of grain boundaries close to the weakest microstructure *SG_D*, *SG_A* and $TJ\_V_{max/ave}$ values is an effective approach to designing materials that are resistant to hydrogen embrittlement.

The statistical approach adopted in this paper identifies the factors that govern hydrogen embrittlement from complex 3D images and presents the characteristics of the weakest polycrystalline microstructure. This leads to a logic-based interpretation of the hydrogen embrittlement behaviour exhibited by complex polycrystalline microstructures and suggests the potential to prevent of hydrogen embrittlement through the optimisation of polycrystalline microstructures. In the future, more effective polycrystalline microstructure optimisation may also be achieved with the aid of 3D image-based deformation and hydrogen diffusion multimodal simulations.

Acknowledgements

This work was funded by JST Core Research for Evolutional Science and Technology (CREST) “Elucidation of nanoscale dynamic behaviour and mechanical property mechanisms for the creation of innovative mechanically functional materials”. The synchrotron radiation experiments were carried out under SPring-8 proposals (2019B2046, 2020A1084, 2020A1796, 2021A1002, 2021B1123, 2022A1005). It was also supported in part by a grant from the Light Metal Educational Foundation, Japan. These are noted and deeply appreciated.

REFERENCES

1) I.M. Robertson, P. Sofronis, A. Nagao, M.L. Martin, S. Wang, D.W. Gross and K.E. Nygren: Metall. Mater. Trans. A **46** (2015) 2323–2341.
2) H. Toda, K. Minami, K. Koyama, K. Ichitani, M. Kobayashi, K. Uesugi and Y. Suzuki: Acta Mater. **57** (2009) 4391–4403.
3) H. Toda, H. Oogo, K. Horikawa, K. Uesugi, A. Takeuchi, Y. Suzuki, M. Nakazawa, Y. Aoki and M. Kobayashi: Metall. Mater. Trans. A **45** (2014) 765–776.
4) H. Toda, T. Inamori, K. Horikawa, K. Uesugi, A. Takeuchi, Y. Suzuki and M. Kobayashi: Mater. Trans. **54** (2013) 2195–2201.
5) T. Tsuru, K. Shimizu, M. Yamaguchi, M. Itakura, K. Ebihara, A. Bendo, K. Matsuda and H. Toda: Sci. Rep. **10** (2020) 1998.
6) H. Fujihara, H. Toda, K. Ebihara, M. Kobayashi, T. Mayama, K. Hirayama, K. Shimizu, A. Takeuchi and M. Uesugi: Int. J. Plast., under review.
7) R. Higa, H. Fujihara, H. Toda, M. Kobayashi, K. Ebihara and A. Takeuchi: J. JILM, accepted.
8) K. Kawano-Miyata: Mater. Sci. Eng. A **858** (2022) 144074.
9) K. Hirayama, H. Toda, D. Fu, R. Masunaga, H. Su, K. Shimizu, A. Takeuchi and M. Uesugi: Corros. Sci. **184** (2021) 109343.
10) K. Shimizu, H. Toda, H. Fujihara, K. Hirayama, K. Uesugi and A. Takeuchi: Eng. Fract. Mech. **216** (2019) 106503.
11) Y.-S. Chen, H. Lu, J. Liang, A. Rosenthal, H. Liu, G. Sneddon, I. McCarroll, Z. Zhao, W. Li, A. Guo and J.M. Cairney: Science **367** (2020) 171–175.
12) N.M. Vlasov and I.I. Fedik: Int. J. Hydrogen Energ. **27** (2002) 921–926.
13) H.L. Mai, X.-Y. Cui, D. Scheiber, L. Romaner and S.P. Ringer: Mater.

Des. **212** (2021) 110283.
14) M. Yamaguchi, K. Ebihara, M. Itakura, T. Tsuru, K. Matsuda and H. Toda: Comput. Mater. Sci. **156** (2019) 368–375.
15) C.J. McMahon: Eng. Fract. Mech. **68** (2001) 773–788.
16) K. Okada, A. Shibata, T. Sasaki, H. Matsumiya, K. Hono and N. Tsuji: Scr. Mater. **224** (2023) 115043.
17) S. Bechtle, M. Kumar, B.P. Somerday, M.E. Launey and R.O. Ritchie: Acta Mater. **57** (2009) 4148–4157.
18) Y. Takahashi, H. Kondo, R. Asano, S. Arai, K. Higuchi, Y. Yamamoto, S. Muto and N. Tanaka: Mater. Sci. Eng. A **661** (2016) 211–216.
19) A. Zafra, G. Álvarez, J. Belzunce, J.M. Alegre and C. Rodrígue: Eng. Fract. Mech. **241** (2021) 107433.
20) X. Xing, J. Gou, F. Li, Y. Zhang, J. Cheng, Y. Wang, J. Liu, G. Cui, Z. Li, P. Zhang, X. Luo and B. Wang: Int. J. Hydrogen Energ. **46** (2021) 36528–36538.
21) H. Toda, H. Li, R. Batres, K. Hirayama and H. Fujihara: Acta Mater. **257** (2023) 119188.
22) H. Toda, K. Hirayama, H. Li, R. Batres, S. Dowon and H. Fujihara: Acta Mater. (2023), submitted.
23) W. Ludwig, P. Reischig, A. King, M. Herbig, E.M. Lauridsen, G. Johnson, T.J. Marrow and J.Y. Buffière: Rev. Sci. Instrum. **80** (2009) 033905.
24) H. Toda: *X-Ray CT, Hardware and Software Techniques*, (Springer Nature Singapore, Singapore, 2021).
25) H. Su, H. Toda, R. Masunaga, K. Shimizu, H. Gao, K. Sasaki, M. Bhuiyan, K. Uesugi, A. Takeuchi and Y. Watanabe: Acta Mater. **159** (2018) 332–343.
26) M.S. Bhuiyan, Y. Tada, H. Toda, S. Hang, K. Uesugi, A. Takeuchi, N. Sakaguchi and Y. Watanabe: Int. J. Fract. **200** (2016) 13–29.
27) H. Toda, E. Maire, Y. Aoki and M. Kobayashi: J. Strain Anal. Eng. Des. **46** (2011) 549–561.
28) H. Su, H. Toda, K. Shimizu, K. Uesugi, A. Takeuchi and Y. Watanabe: Acta Mater. **176** (2019) 96–108.
29) J. Evans: *Straightforward Statistics for the Behavioral Sciences*, (Brooks/Cole Publishing, Pacific Grove, CA, 1996).
30) T. Ogura, S. Hirosawa and T. Sato: Sci. Technol. Adv. Mater. **5** (2004) 491–496.
31) T. Tsuru, M. Yamaguchi, K. Ebihara, M. Itakura, Y. Shiihara, K. Matsuda and H. Toda: Comput. Mater. Sci. **148** (2018) 301–306.
32) K. Shimizu, H. Toda, K. Hirayama, H. Fujihara, T. Tsuru, M. Yamaguchi, A. Bendo, K. Matsuda, M. Uesugi and A. Takeuchi: In preparation.
33) H.K. Birnbaum, C. Buckley, F. Zeides, E. Sirois, P. Rozenak, S. Spooner and J.S. Lin: J. Alloy. Compd. **253–254** (1997) 260–264.
34) H. Toda: *X-ray CT: Practical Application of Tomography in Industry and Science & Engineering*, (Kyoritsu Shuppan Co. LTD., Japan, 2019).

Appendix

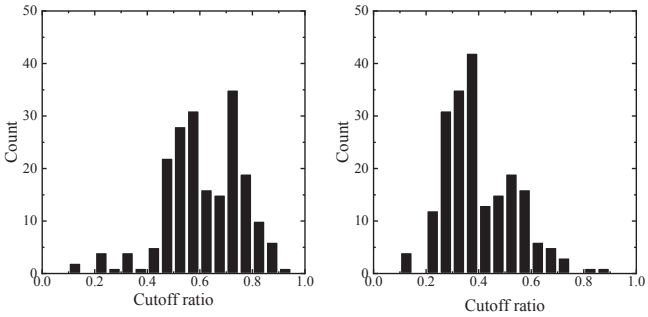

(a) Grain cutoff ratio before correction. (b) Grain cutoff ratio after correction.

Fig. S1 Histograms of grain cutoff ratio (a) before and (b) after correction.

Table S1 A list of the parameters for surface grain boundary (SG), two surface grains that form a surface grain boundary (GP), and three surface grains that form as surface grain boundary triple junction (TJ) that were used for the statistical analyses.

Categories	Microstructural parameters	Remarks
I. SG	*SG_A*	Grain boundary area
(5 parameters)	*SG_D*	Grain boundary orientation
	SG_R	Grain boundary aspect ratio
	SG_C	Grain boundary curvature
	SG_P	Density of pore around grain boundary
II. GP	*GP_V*	Grain volume ratio
(16 parameters)	*GP_S*	Ratio of grain removal ratio between 2 grains
	GP_C	Ratio of mean curvature of grains
	GP_f1, GP_f2, GP_f3	Ratio of Spherical deviation of grains
	GP_f4, GP_f5, GP_f6	Ratio of Cubic deviation of grains
	GP_AR1, GP_AR2, GP_AR3	Ratio of Aspect ratio of grains
	GP_Tyl	Ratio of Taylor factors
	GP_Sch	Ratio of Schmid factors
	GP_Ori	Misorientation
	GP_G	Sum of the number of neighboring grains
III. TJ	TJ_V_{max}	Max. grain vol. among 3 grains around TJ line
(45 parameters)	TJ_S_{max}	Max. grain removal ratio among 3 grains around TJ line
	TJ_C_{max}	Max. mean grain curvature among 3 grains around TJ line
	TJ_f1_{max}, TJ_f2_{max}, TJ_f3_{max}	Max. spherical deviation among 3 grains around TJ line
	TJ_f4_{max}, TJ_f5_{max}, TJ_f6_{max}	Max. cubic deviation among 3 grains around TJ line
	TJ_R1_{max}, TJ_R2_{max}, TJ_R3_{max}	Max. aspect ratio of grain among 3 grains around TJ line
	TJ_Tyl_{max}	Max. Taylor factor among 3 grains around TJ line
	TJ_Sch_{max}	Max. Schmid factor among 3 grains around TJ line
	TJ_Ori_{max}	Max. misorientation among 3 grains around TJ line
	TJ_V_{ave}	Ave. grain volume among 3 grains around TJ line
	TJ_S_{ave}	Ave. grain removal ratio among 3 grains around TJ line
	TJ_C_{ave}	Ave. mean curvature among 3 grains around TJ line
	TJ_f1_{ave}, TJ_f2_{ave}, TJ_f3_{ave}	Ave. spherical deviation among 3 grains around TJ line
	TJ_f4_{ave}, TJ_f5_{ave}, TJ_f6_{ave}	Ave. cubic deviation among 3 grains around TJ line
	TJ_R1_{ave}, TJ_R2_{ave}, TJ_R3_{ave}	Ave. aspect ratio of grain among 3 grains around TJ line
	TJ_Tyl_{ave}	Ave. Taylor factor among 3 grains around TJ line
	TJ_Sch_{ave}	Ave. Schmid factor among 3 grains around TJ line
	TJ_Ori_{ave}	Ave. misorientation among 3 grains around TJ line
	$TJ\_V_{max/ave}$	Max./ave. of grain vol. among 3 grains around TJ line
	$TJ\_S_{max/ave}$	Max./ave. value of grain removal ratio around TJ line
	$TJ\_C_{max/ave}$	Max./ave. value of mean curvature of grain around TJ line
	$TJ\_f1_{max/ave}$, $TJ\_f2_{max/ave}$, $TJ\_f3_{max/ave}$	Max./ave. spherical deviation of grain around TJ line
	$TJ\_f4_{max/ave}$, $TJ\_f5_{max/ave}$, $TJ\_f6_{max/ave}$	Max./ave. value of cubic deviation of grain around TJ line
	$TJ\_R1_{max/ave}$, $TJ\_R2_{max/ave}$, $TJ\_R3_{max/ave}$	Max./ave. value of aspect ratio of grain around TJ line
	$TJ\_Tyl_{max/ave}$	Max./ave. value of Taylor factor around TJ line
	$TJ\_Sch_{max/ave}$	Max./ave. value of Schmid factor around TJ line
	$TJ\_Ori_{max/ave}$	Max./ave. value of misorientation around TJ line